Supplementary Material

Emergent collective behavior of active Brownian particles with visual perception

Rajendra Singh Negi, Roland G. Winkler, and Gerhard Gompper
Theoretical Physics of Living Matter, Institute of Biological Information Processing and Institute for Advanced Simulation, Forschungszentrum Jülich, D-52425 Jülich, Germany.
(Dated: July 15, 2022)

S-I. POLARITY FIELD OF AGGREGATES

In order to characterize the internal structure of close-packed structures and droplet-like aggregates, we consider the polarity field $\mathbf{p} = \langle \mathbf{e} \rangle$ as a function of radial distance r from their centers of mass, where $\mathbf{e}$ is the instantaneous orientation vector of the ABPs. Averages are taken over time, and spatially within a square grid with lattice constant $\sqrt[6]{2}\sigma$. Configurations are ignored which occur for less than 500 times (10%) out of all recorded configurations.

Figure S1 shows the polarity field for two typical aggregate structures within the phase diagram, Fig. 9 of the main text, for the close-packed HCP phase at high Pe in Fig. S1(a,c)), and in the lose-packed aggregate phase at low Pe in Fig. S1(b,d)). Closed-packed structures and dense aggregates generally appear for particles with larger vision angle θ, so that particles near the aggregate center see an isotropic environment, which results in a very small time-averaged polarity. On the other hand, particles at the periphery always try to orient toward the center-of-mass of the sensed density distribution, so that $|\mathbf{p}|$ of the polarity field has a maximum there. The large particle polarization $|\mathbf{p}|$ at the edge prevents the cluster from breaking apart and results in the formation of very stable close-packed structures. For the lose-packed aggregate phase, the polarity is again very small at the center, due to the presence of other particles all around a given particles, and over time its motion is isotropic, while particles at the periphery are oriented toward the center of mass and have a high polarity.

We employ the radial distribution function $|\mathbf{p}|(r)$ to estimate the cluster size. For the lose-aggregate case of Fig. S1(b),(d), the radius is found to be $R_{agg} \simeq 20\sigma$, whereas for the close-packed structures it is $R_{HCP} \simeq 16\sigma$ (Fig. S1(a),(c)). The smaller value for the HCP aggregate is expected, because of the very compact packing of particles and a larger internal density.

S-II. PHASE DIAGRAMS

Since the minimal cognitive active particle model contains at least five relevant parameters — the activity Pe, the vision angle θ, the maneuverability Ω, the vision cut-off radius R_0, and the packing fraction Φ — it is very difficult to obtain a detailed picture of the whole phase diagram. To achieve an overview of the principal behavior, we have constructed two-dimensional cuts through the phase space in several orthogonal planes. The results are displayed in Fig. 9 of the main text, and in Fig. S2.

Figure S2(a) shows the effect of the characteristic vision range R_0. With increasing R_0 (at fixed vision angle θ) the number of "visible" iABPs increases, which enhances the possibility to locate and move toward existing aggregates of other iABPs. Thus, even for small vision angles i.e. $\theta = \pi/5$ at $R_0 = 4.5\sigma$, iABPs are able to sense enough particles to form close-packed structures, whereas for $R_0 = 1.5\sigma$ the system is still in the lose-aggregate phase. Thus, the vision range R_0 together with the vision angle plays a crucial role in structure formation.

Figure S2(b) displays the effect of maneuverability Ω on the formation of different phases. With increasing Ω, an iABP can react more decisively on the sensed density distribution and move toward its center of mass, which implies an enhanced ability to form clusters and aggregates even at small vision angles. A similar phase diagram is shown in Fig. 5(b) of the main text – for a lower packing fraction $\Phi = 0.00785$ and a much larger Péclet number $Pe = 200$. From both phase diagram, we conclude that a stronger maneuverability favors the formation of aggregates or close-packed structures, even at lower vision angles. A small maneuverability obviously implies that thermal fluctuation in particle orientation dominate over the tendency to reorient toward the sensed direction, so that particle orientations remain random and the dilute phase prevails.

Figure S2(c) shows the impact of self-propulsion activity Pe on the structure formation. This phase diagram should be compared with the low-Pe part of the phase diagram of Fig. 9 in the main text, but displays the phase behavior for a factor 2 larger packing fraction. The behavior is found to be very similar, except that now the phase boundaries are shifted to somewhat lower values of the vision angle.

S-III. STRUCTURAL PROPERTIES

A. Hexagonal order parameter

In order to distinguish between aggregates with closed-packed structures and those with more fluid-like structure, we employ the hexagonal order parameter $|q_6|^2$,

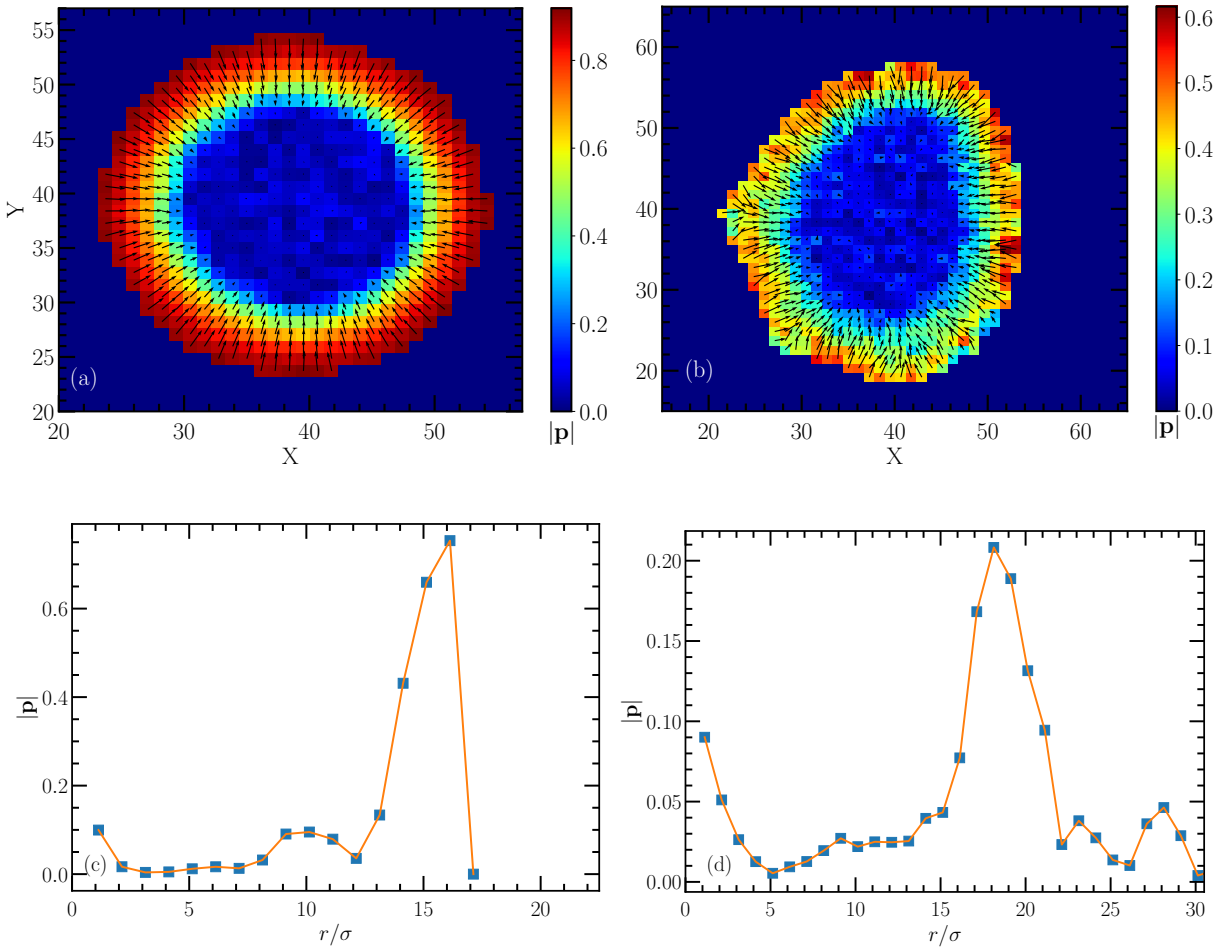

FIG. S1. (a),(b) Polarity field $\mathbf{p}$ and (c),(d) corresponding radial distribution functions $|\mathbf{p}|(r)$, for (a),(c) the HCP phase at the Péclet number $Pe = 200$, the vision angle $\theta = \pi/3$ (Fig. 8(b)), and (b),(d) the lose-aggregate phase at $Pe = 20$ and $\theta = \pi/10$ (comparable to Fig. 8(d)). In (a), no iABPs are outside of the radius $r/\sigma \approx 17$. In both cases, the maneuverability $\Omega/D_R = 62.5$, the vision range $R_0 = 1.5\sigma$, and the packing fraction $\Phi = 0.0785$. The color bar indicates the magnitude of the polarity.

with

$$q_6 = \frac{1}{6} \sum_{j \in N_6^k} e^{i6\vartheta_{kj}} \tag{S-1}$$

where N_6^k is the set of six nearest neighbours of swimmer k , ϑ is the angle between the vectors connecting the centers of particles j and k, and the x axis . For an hexagonal lattice, $|q_6|^2 = 1$. Figure S3 displays the hexagonal-order-parameter distribution for various vision angles at $Pe = 8$ and the packing fraction $\Phi = 0.0157$ (compare phase diagram in Fig. S2(c)). This clearly demonstrates the existence of hexagonally packed structures for vision angles $\theta \geq \pi/4$, where a maximum is obtained at $|q_6|^2 \simeq 1$. For $\theta \leq \pi/6$, this peak is not present. Thus, this is a convenient criterion to distinguish the HCP phase from other phases.

B. Pair correlation function

The radial pair-correlation function $g(r)$ characterizes the local structure of a fluid. It measures the number of particles at a distance r form a given particle, divided by the number of particles at the same distance for a homogeneous distribution of the same density. Figure S4 displays the pair correlation function for a low packing fraction $\Phi = 0.00785$. A peak at the nearest-neighbor distance appears, which is much higher than the peak in a corresponding passive system (which at this low density has nearly constant $g(r)$). Thus, even our dilute phase ($\theta = \pi/10$) displays significant clustering and inhomogeneities. For worms, with vision angles $\theta = \pi/7$ and $\pi/6$, small peaks close to $r = 2.4\sigma$, 3.6σ, and 4.8σ are visible, in addition to the large nearest-neighbor peak at $r = 1.2\sigma$. These small peaks signal the single-file structure of worms with a regular spacing between the

particles. Finally, for the worm-aggregate coexistence, with vision angle $\theta = \pi/4$, the pair correlation function is dominated by the hexagonal packing of the particles in the aggregates.

S-IV. CLUSTER GROWTH

The average cluster size $C(t)$ as a function of time is presented in Fig. 13(a) of the main text, for various Pe in the range $1 \leq Pe \leq 20$ for the vision angle $\theta = \pi/2$ and packing fraction $\Phi = 0.157$. We supplement this here by showing in Fig. S5(a) the time-dependence of the average cluster size for various vision angles θ at $Pe = 8$. For vision angles $\theta \geq \pi/6$, we obtain two power-law regimes, $C(t) \sim t^{z_k}$ $(k = 1, 2)$, as in Fig. 13(a) at various Pe. In the short-time regime $1 < D_R t < 10$, before the iABPs reach the active diffusive time regime, the growth exponent z_1 depends on the vision angle as $\theta^{1/5}$, see Fig. S5(b)). For longer times $D_R t \geq 10$, $C(t)$ crosses assumes a second power-law regime $C(t) \sim t^{z_2}$, where the exponent $z_2 = 1/4$ is independent of θ. The time-independent prefactor of $C(t)$ depends on θ and Pe.

We also consider the concentration $P_n(t)$ of cluster sizes containing n iABPs (Sec. 5 of the main text), see Fig. S5(c). The time at which the concentration assumes a maximum is found to depend on θ as $\theta^{\kappa/4}$, so that together with the results displayed in Fig. 13(b) of the main text, we obtain

$$\tau_p D_r = 5.5(n/Pe)^{\kappa}\theta^{-\kappa/4}, \tag{S-2}$$

with $\kappa = 6/5$, as shown in Eq. (16) of the main text.

S-V. FINITE-SIZE EFFECTS

In order to investigate to which extent our results for cluster growth might be affected by finite-size effects, we determine the the average cluster size $C(t)$ (at packing fraction $\Phi = 0.157$, maneuverability $\Omega/D_R = 62.5$, Péclet numbers $Pe = 10$ and 16, and vision angle $\theta = \pi/2$) also for larger particle numbers $N = 1250$ and $N = 2500$. Figure S6 demonstrates that the growth of the average cluster size is independent of system size. This is to be expected, as in the consider time range, the average cluster size is much smaller than the total number N of particles. Thus, the results fro the power law regime remain the same as in Fig. 13(a) of main text.

The finite-size behavior of the phase behavior is much more difficult to investigate, as it would require a determination of the full phase diagram for different system sizes. We therefore focus on the stability of worm-aggregate coexistence, as this phase seems to be potentially most sensitive to finite-size effects. This is done by performing simulations for various particle numbers $N = 100, 200, ..., 1000$, at a point where the worm-aggregate coexistence is found in Fig. 5(a) of the main

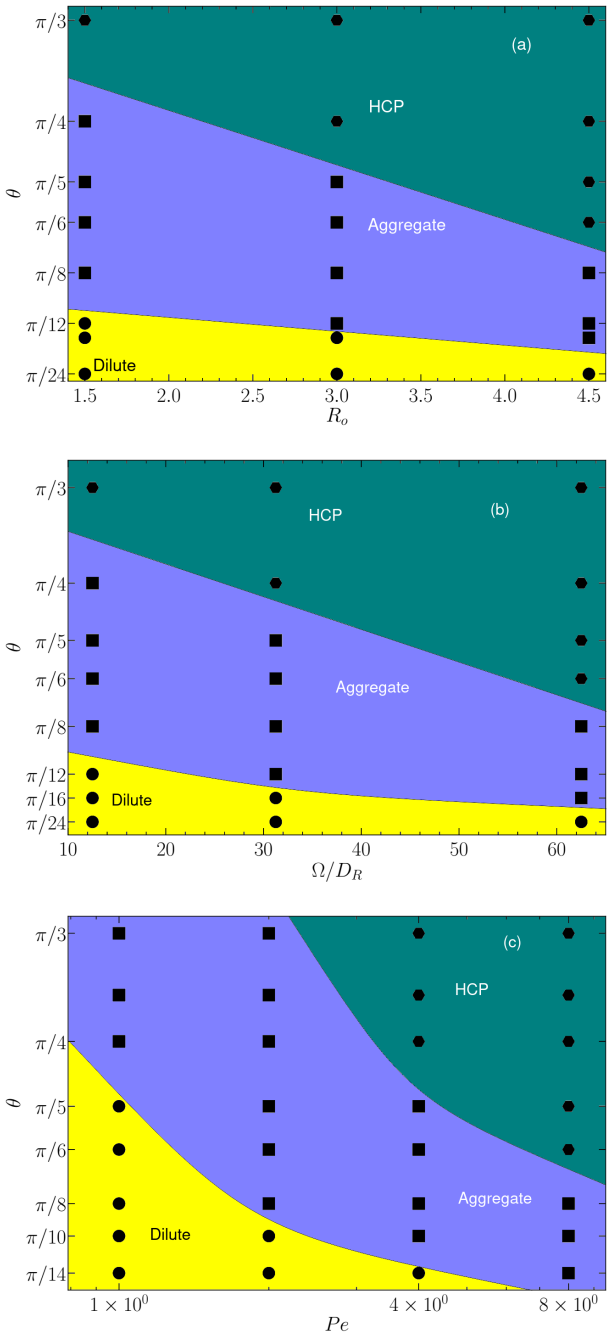

FIG. S2. Phase diagrams. (a) Vision angle θ as a function of the cutoff radius R_0 at $\Omega = 1$, $\Phi = 0.0785$, $Pe = 10$; (b) Vision angle θ as a function of the maneuverability Ω for R_0, packing fraction $\Phi = 0.0785$ and activity $Pe = 10$; (c) activity Pe versus vision angle θ, at fixed maneuverability $\Omega/D_R = 62.5$, vision cutoff radius $R_0 = 1.5\sigma$, and packing fraction $\Phi = 0.157$. The individual phases are indicated by different colors and symbols. HCP: navy ⬢, aggregate: purple ■, dilute: yellow ●. The indicated "phase" boundaries are guides to the eye.

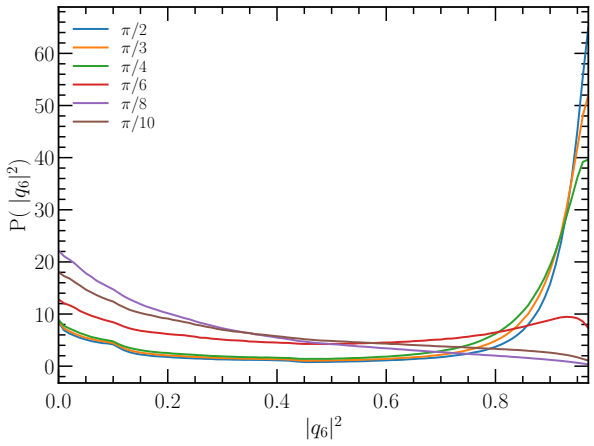

FIG. S3. Hexagonal order parameters function for various vision angle θ , $Pe = 8$, and the packing fraction $\Phi = 1.57 \times 10^{-1}$.

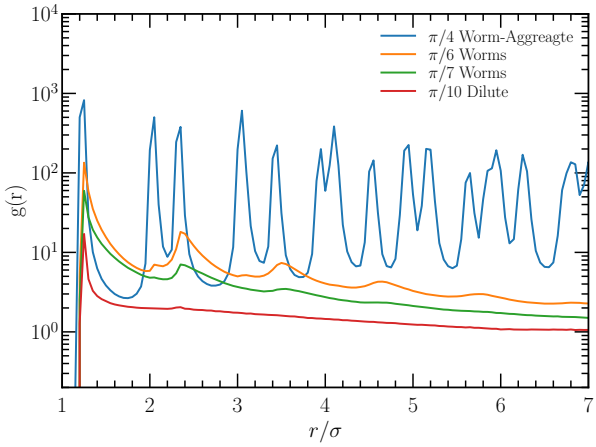

FIG. S4. Pair correlation function $g(r)$ of iABPs at $Pe = 200$, $\Omega/D_R = 62.5$, vision range $R_0 = 1.5\sigma$, and the packing fraction $\Phi = 0.00785$.

text, i.e. for $Pe = 200$, $\Omega/D_R = 62.5$, and packing fraction $\Phi = 7.85 \times 10^{-3}$. Figure S7 shows snapshots of worm-aggregate phase at two particles number $N = 625$ and 1000, in both cases normalized by the linear system size. The structure looks almost identical, just the size of cluster and worms increases roughly linearly with increasing N. This indicates that finite-size effects are small. Of course, phase boundary may shift slightly as the system size is varied.

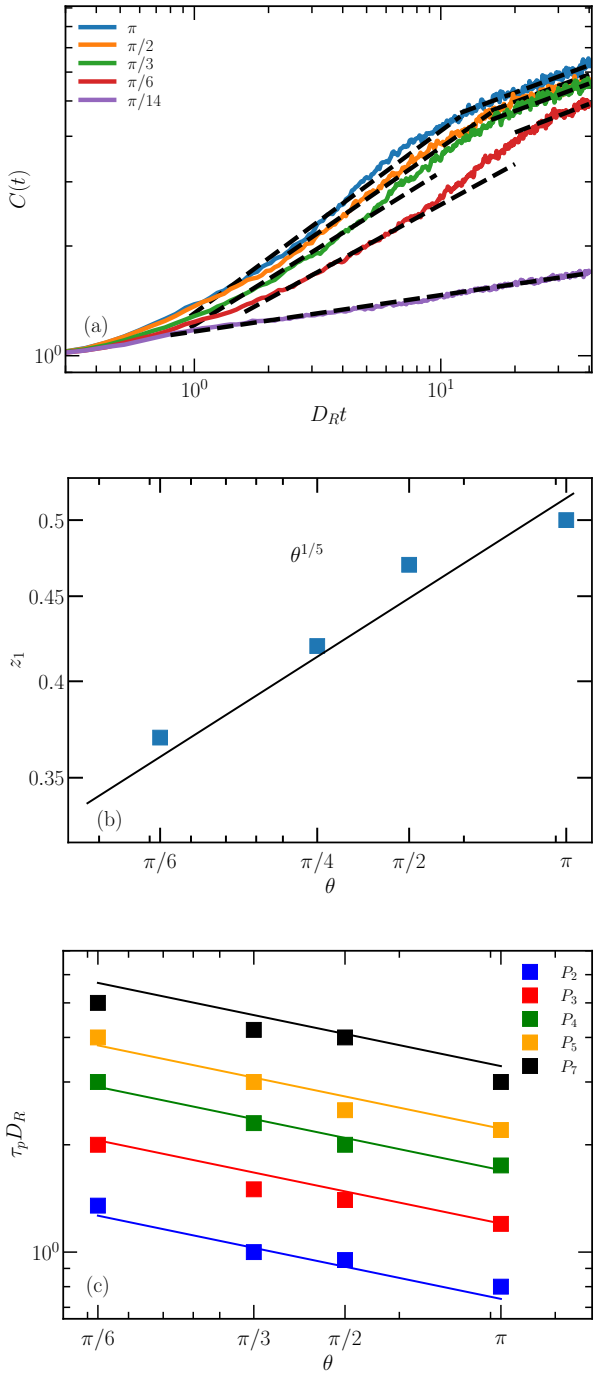

FIG. S5. (a) Average cluster size as a function of time for various vision angle θ, $Pe = 8$, and the packing fraction $\Phi = 0.157$. (b) Growth exponent z_1 as a function of Pe. (c) Characteristic times of the maxima of $P_n(t)$ as a function of θ. The fitted lines correspond to Eq. S-2, whereas the squares represent simulation results.

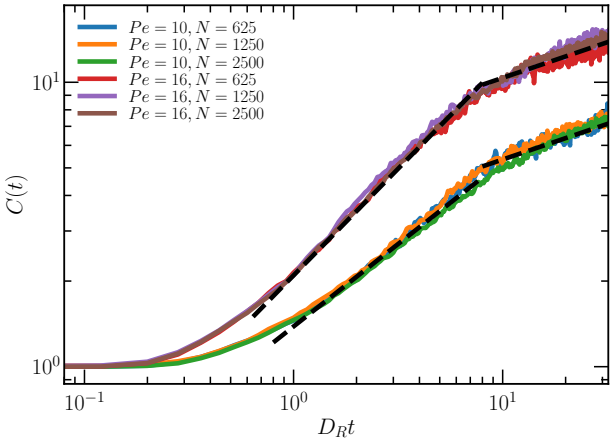

FIG. S6. Average cluster size $C(t)$ as a function of scaled time $D_R t$, for various system size as indicated, for vision angle $\theta = \pi/2$, and the packing fraction $\Phi = 0.157$.

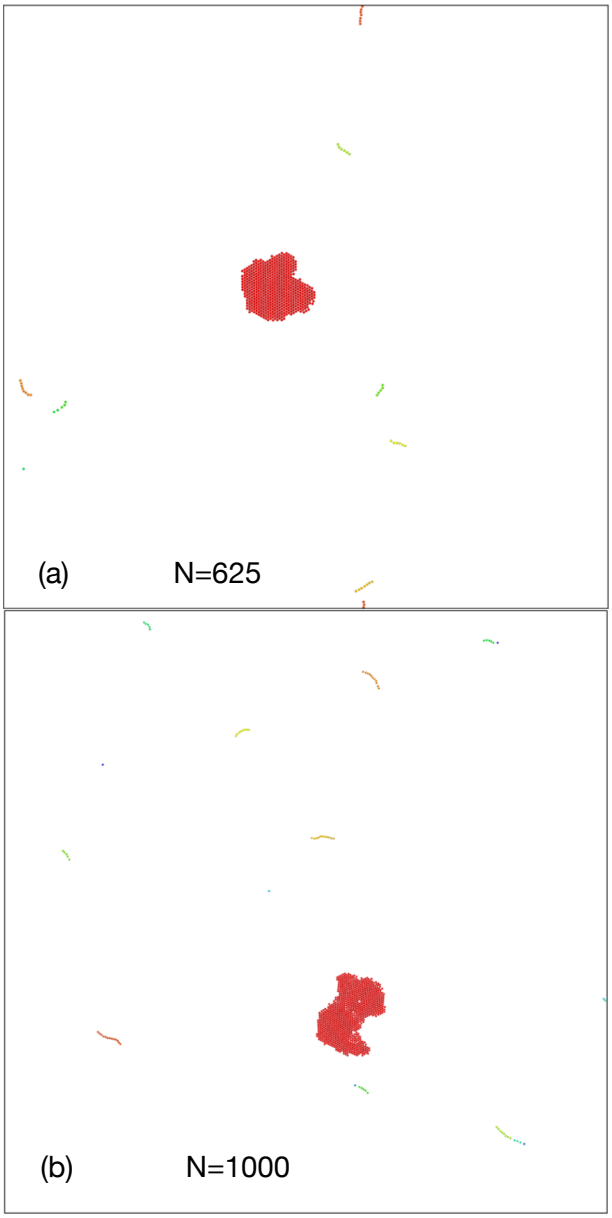

FIG. S7. Snapshots of iABP structures for particle numbers (a) $N = 625$ (b) $N = 1000$, displaying worm-aggregate coexistence, at vision angle $\theta = \pi/4$, for Péclet number $Pe = 200$, maneuverability $\Omega/D_R = 62.5$, and packing fraction $\Phi = 7.85 \times 10^{-3}$. Compare phase diagram in Fig. 5(a) of the main text.

S-VI. MOVIES

- **Movie M1** Very slow rotational dynamics of the hexagonally close-packed (HCP) aggregate at $Pe = 200$, $\theta = \pi/2$, $\Omega/D_R = 62.5$, $R_0 = 1.5\sigma$, and $\phi = 0.00785$.

- **Movie M2** Dynamics of the worm phase, with splitting, merging, and collisions of worms at $Pe = 200$, $\theta = \pi/5$, $\Omega/D_R = 62.5$, $R_0 = 1.5\sigma$, and $\phi = 0.00785$. Colors represent different worms.

- **Movie M3** Worm-aggregate coexistence, with worms splitting and merging with each other as well as aggregates at $Pe = 100$, $\theta = \pi/8$, $\Omega/D_R = 62.5$, $R_0 = 1.5\sigma$, and $\phi = 0.0785$.

- **Movie M4** In the dispersed cluster phase, iABPs form small short-lived clusters at $Pe = 40$, $\theta = \pi/12$, $\Omega/D_R = 62.5$, $R_0 = 1.5\sigma$, and $\phi = 0.0785$. Particles in green are not part of any cluster.

- **Movie M5** In the aggregate phase, a fluid cluster is comprised of various small and fluctuating clusters at $Pe = 10$, $\theta = \pi/12$, $\Omega/D_R = 62.5$, $R_0 = 1.5\sigma$, and $\phi = 0.0785$.

- **Movie M6** Cluster growth process. The initially homogeneously distributed iABPs start to form dimers, trimers, etc., which merge in the course of time. $Pe = 8$, $\theta = \pi/6$, $\Omega/D_R = 62.5$, $R_0 = 1.5\sigma$, and $\phi = 0.157$.